

Hyperbolic embedding of brain networks as a tool for epileptic seizures forecasting

Martin Guillemaud*

*Paris Brain Institute (ICM), CNRS, Inserm, Sorbonne University,
Inria-Paris. Pitié Salpêtrière University Hospital. Paris, France*

Louis Cousyn* and Vincent Navarro

*Paris Brain Institute (ICM), Sorbonne Université, CNRS UMR, Inserm.
AP-HP, Department of Neurology, Epilepsy Unit,
Center of Reference for Rare Epilepsies, ERN EPICARE,
Pitié Salpêtrière University Hospital, Paris, France*

Mario Chavez

CNRS, Pitié Salpêtrière University Hospital. Paris, France

(Dated: June 21, 2024)

The evidence indicates that intracranial EEG connectivity, as estimated from daily resting state recordings from epileptic patients, may be capable of identifying preictal states. In this study, we employed hyperbolic embedding of brain networks to capture non-trivial patterns that discriminate between connectivity networks from days with (preictal) and without (interictal) seizure. A statistical model was constructed by combining hyperbolic geometry and machine learning tools, which allowed for the estimation of the probability of an upcoming seizure. The results demonstrated that representing brain networks in a hyperbolic space enabled an accurate discrimination (85%) between interictal (no-seizure) and preictal (seizure within the next 24 hours) states. The proposed method also demonstrated excellent prediction performances, with an overall accuracy of 87% and an F1-score of 89% (mean Brier score and Brier skill score of 0.12 and 0.37, respectively). In conclusion, our findings indicate that representations of brain connectivity in a latent geometry space can reveal a daily and reliable signature of the upcoming seizure(s), thus providing a promising biomarker for seizure forecasting.

I. INTRODUCTION

In the last decades, complex networks have provided an increasingly challenging framework for the study of connected systems (from social sciences to biology and physics), based on the interplay between the wiring architecture and the dynamical properties of the coupled elements [1]. In neurosciences, the representation of brain networks as graphs allows to better describe their non-trivial connectivity properties in a compact and objective way [2, 3]. In this mapping of brain data (e.g. scalp or intracranial electroencephalography or magnetoencephalography) to networks, nodes usually represent brain regions or recording sites (e.g., electrodes, sensors), and edges or links indicate functional connections between them, based on an estimated statistical relationship between the recorded signals. Regardless of the modality of acquisition, the use of graph analysis in neurosciences has become essential to characterize pathological or physiological states in terms of connectivity brain networks [2–4]. The application of different graph metrics, including node’s degree, centrality, communicability, and efficiency, has yielded insights into brain function in both healthy and pathological conditions [4].

Epilepsy is a neurological disorder nowadays conceptualized as a network disease with functionally and/or structurally aberrant connections on virtually all spatial scales [5]. According to this concept, a large-scale epileptic network comprises brain areas that can generate and sustain normal and physiological dynamics during the seizure-free interval, and are mainly involved in the generation, maintenance, spread, and termination of pathophysiological activities such as seizures [5, 6]. Network connectivity analysis in epilepsy has provided valuable information on seizure onset and propagation, as well as on the functional organization of the brain during the seizure-free interval [6]. During seizures, brain networks have been found to display a more regular structure with less variability [5, 6]. Nevertheless, current representations of brain networks fail to provide reliable biomarkers to predict seizure onset or to estimate a risk of seizure occurrence. [5–7].

Embedding (or vector space) methods identify a lower-dimensional space in which high-dimensional complex data can be represented. Modern dimensionality reduction methods learn similarities and proximities between points distributed over a hidden manifold in a multidimensional feature space. These methods then preserve, embed, and visualize the data in a low-dimensional space. Although Euclidean geometry serves as a standard framework for studying our physical reality, an increasing body of evidence suggests that non-Euclidean geometries are a more appropriate framework for capturing non-trivial

* These authors contributed equally to this work

features (e.g., hierarchical or multiscale structure) often observed in different biological networks, such as the olfactory space, cell development data, single-cell sequencing data, and the brain connectivity [8].

The prevailing network embedding methodologies assume a zero-curvature (or flat) space and evaluate the distance between embedded nodes according to Euclidean metrics. These approaches, however, are limited when dealing with complex hierarchical structures, as the resulting pairwise distances in the embedded spaces are substantially distorted [8]. In network analysis, the question of whether it exists a hidden (latent) non-Euclidean geometry from which complex connectivity emerges has recently attracted the attention of the scientific community and is getting more and more ground [9, 10]. Recently, spaces with negative curvature (hyperbolic geometries) have attracted a lot of attention as they enable low-distortion embeddings of hierarchical or multi-scale connectivity structures [8]. The possibility to find an effective congruency between brain network characteristics and its representation in hyperbolic spaces offers thus the possibility to understand its structure and address the study of brain organization in a novel and promising framework. In some cases, endowed metrics of such spaces allow the use of machine learning tools to perform statistical analysis of the embedded points (e.g. clustering, prediction, ...) [11].

Previous studies [12, 13] showed that brain connectivity matrices, estimated from intracranial electroencephalography (EEG) recordings, allowed the identification of preictal states. In the present study we used network embedding methods to predict the risk of seizure occurrence. Our approach aimed at exploring hyperbolic geometry to represent functional brain networks of patients with epilepsy, and to work in a more adapted space representation to unveil patterns that could potentially result in robust biomarkers for seizure forecasting.

II. MATERIAL AND METHOD

A. Data acquisition

The EEG dataset used in this study was previously presented in [14]. Briefly, daily 10-minute resting-state intracranial EEG recordings were obtained in 10 patients (mean age 30.7 years) with drug-resistant focal epilepsy from January 2019 to July 2021 in the Epilepsy Unit of the Pitié-Salpêtrière Hospital (Paris, France). The study was conducted in accordance with the Helsinki Declaration and approved by an institutional review board (project C11-16 and C19-55 of the French National Institute of Health and Medical Research sponsor).

The mean number of daily recordings per patient was 11. Each daily recorded period was labeled as “preictal” in case an electro-clinical seizure occurred in the next 24 hours, or “interictal” otherwise. Connectivity graphs were derived from matrices of phase locking values (PLV)

estimated between pairs of EEG signals during 20-second non-overlapping epochs (resulting in 30 connectivity matrices per day). Synchrony (PLV) values were obtained in the typical EEG frequency bands: delta (δ) 1-4 Hz, theta (θ) 4-8 Hz, alpha (α) 8-13 Hz, beta (β) 13-30 Hz, low gamma (low γ) 30-49 Hz and high gamma (high γ) 51-90 Hz. Only contacts in the gray matter were considered and a bipolar montage between adjacent contacts was applied.

B. Hyperbolic embedding of brain networks

In this study, we employed hyperbolic geometrical space for the representation of brain networks. Compared with graph mappings in Euclidean spaces, hyperbolic embeddings exhibit low distortion and can unfold network properties, such as clustering or hierarchical community structure [15–17], which could reveal key structural principles underlying the organization of the brain. The main steps required to embed the brain networks into this geometric space include: i) filtering the connectivity matrix, ii) embedding the network into the geometric space, and iii) aligning the embedding in the hyperbolic space.

Networks filtering. The initial stage of network embedding consists of filtering the PLV matrices by applying a threshold to cancel a percentage of the weakest values. Here, we followed Ref. [18], and the synchrony matrices were filtered such that the final networks reached a predetermined mean degree, fixed here to 4. Although a spanning tree filter could be applied to ensure a unique acyclic subgraph that connects all nodes [19], here we preferred the method of Ref. [18] as it emphasizes the intrinsic global and local properties of the network, while preserving its sparsity.

Networks embedding. Hyperbolic embedding methods are becoming increasingly prevalent in the literature on neural circuits [17, 20–22]. Hyperbolic geometry studies metric spaces with a constant negative curvature that do not conform to Euclidean geometry. Such embedding methods typically project the nodes of a network onto a hyperboloid, which can then be projected onto a two-dimensional hyperbolic space model, such as the Poincaré disk or the so-called Klein model disk. Methods for mapping a network into the hyperbolic disk essentially belong to two families [23, 24]: generative model-based (e.g., Mercator [25]) and machine learning-based. Here, we used the coalescent embedding method [26] to project the brain networks onto the Poincaré disk \mathbb{D} . The method belongs to the second family, and we choose it for its remarkable versatility and especially its computational speed [27].

In a nutshell, the method first adjusts the network’s edges’ weights, giving more weight to those connections that play a greater role in information transmission. Next, the graph is projected onto a 2-dimensional space using a non-linear dimension reduction method such as

Isomap or the Laplacian eigenmaps [28]. Here we employed the technique of Laplacian Eigenmaps as it is computationally efficient and it optimally preserves nodes' local neighborhood information [29]. At this stage, all nodes have polar coordinates (r, θ) in the 2-dimensional space. The nodes undergo an equidistant adjustment in which all radii are set to 1 and the angular coordinates of the nodes are modified while maintaining their angular order within the circle. Finally, each vertex is assigned a radius based on its rank in the order of increasing degree. The radius of a node is thus related to its popularity, while the angular distance between two nodes is related to their topological similarity.

In the Poincaré disk, the hyperbolic distance $\text{dist}_{hyp}(i, j)$ between each pair of nodes i and j , assigned with radii (r_i, r_j) and angles (θ_i, θ_j) with coordinates (r_i, θ_i) and (r_j, θ_j) , is computed according to the hyperbolic law of cosines[30]:

$$\begin{aligned} \cosh \text{dist}_{hyp}(i, j) &= \cosh r_i \times \cosh r_j \\ &- \sinh r_i \times \sinh r_j \times \cos(\pi - |\pi - |\theta_i - \theta_j||) \end{aligned} \quad (1)$$

Graphs alignment. Prior to comparing groups of embedded networks, it was necessary to correct or align the embeddings, as a minor perturbation could result in a random angular offset to the nodes' positions in the hyperbolic disk. A minor connectivity perturbation may thus result in two embeddings with the same similarities between nodes but with a different structure regarding the coordinates in the disk. [31]. To address this issue, a small rotation angle between two embeddings was added such that the following hyperbolic similarity score was minimized:

$$\Gamma_{\text{similarity}} = \sum_{i=0}^N \text{dist}_{hyp}(\text{Pos}_o(i), \text{Rot}_\theta[\text{Pos}_p(i)]) \quad (2)$$

where $\text{Pos}_o(i)$ and $\text{Pos}_p(i)$ denote the positions of the node i in the first (or reference) and second hyperbolic disk, and $\text{Rot}_\theta[\cdot]$ indicates a rotation in the Poincaré's disc with an angle $\theta \in [-\pi, \pi[$. In order to facilitate comparison in subsequent steps, all networks from both groups were aligned using the same reference network.

C. Hyperbolic score disk calculation

Our approach aimed at identifying disparities between preictal and interictal connectivity patterns in the hyperbolic embedding of the brain networks. To achieve this, we first defined a Gaussian model in the hyperbolic space for each embedded node of the interictal networks (reference group). Subsequently, the proximity of nodes from a network to the interictal connectivity can be evaluated through the hyperbolic error [32]. Learning from the interictal networks, the most representative data in the dataset, alleviates the bias related to class-imbalanced training datasets. For each network in both the preictal

and interictal group, the position of each node in the hyperbolic disk was examined and the node was assigned the value of the hyperbolic Gaussian probability density function of this node in the reference interictal group. The principle is illustrated in Fig. 1.

It should be noted that hyperbolic space is a Riemannian manifold, rather than a vector space. As a result, the basic operations of vectors and matrices are either intractable or not explicitly defined in hyperbolic spaces. Nevertheless, for a point $z \in \mathbb{D}$, the tangent space at z , denoted by $T_z\mathbb{D}$, is an inner product space, which contains the tangent vector with all possible directions at z . We can transport points in \mathbb{D} to the tangent space $T_z\mathbb{D}$, and apply most vector operators (average, gradients, ...) within this Euclidean subspace, and then project back the result to the disk. Transportation between $T_z\mathbb{D}$ and \mathbb{D} can be achieved via the logarithmic and exponential maps, Log_z and Exp_z , respectively, defined in Appendix A 1.

To estimate the hyperbolic error we first projected each node i from all reference (interictal) networks into a tangent space to estimate their barycenter \hat{z}_i with the algorithm detailed in Appendix A 2. For each node i^k from network k in the second group, with coordinates (x_i^k, y_i^k) in the hyperbolic disk \mathbb{D} , the score value was calculated using the following formula:

$$\begin{aligned} \text{Score}(i^k) &= P_i^{\text{ref}}(W_i^k) \\ &= \frac{1}{\sqrt{(2\pi)^2 \|V_i\|}} \text{Exp} \left[-\frac{1}{2} W_i^k T V_i^{-1} W_i^k \right] \end{aligned} \quad (3)$$

where

$$W_i^k = \begin{bmatrix} \text{Real}(\text{Log}_{\hat{z}_i}(x_i^k + jy_i^k)) \\ \text{Im}(\text{Log}_{\hat{z}_i}(x_i^k + jy_i^k)) \end{bmatrix}$$

denotes the projected coordinates of node i^k from network k in the tangent space centered on \hat{z}_i (the hyperbolic barycenter of nodes i in the reference group). $\|V_i\|$ is the determinant of covariance matrix V_i of the nodes i from the reference embeddings projected in the tangent space centered on \hat{z}_i , and j denotes the imaginary unit $j = \sqrt{-1}$. It should be noted that the barycenter of the distribution of the set of points projected in this tangent space has coordinates $(0, 0)$.

$P_i^{\text{ref}}(W_i^k)$ is the hyperbolic Gaussian model of nodes i in the reference interictal networks, estimated at the position of the i^{th} node of a network k . Once the scores of all the nodes have been calculated, the disk is discretized with a grid, and the errors of the nodes can be interpolated in the whole disk (one for each network). To perform the interpolation, the scores of the $n = 8$ nearest nodes to each pixel of the grid are averaged, with the weights being inversely proportional to the distances between the pixel and the nodes' positions on the disk. This results in a Hyperbolic Score Disk (HDS) for each network (see Fig. 1).

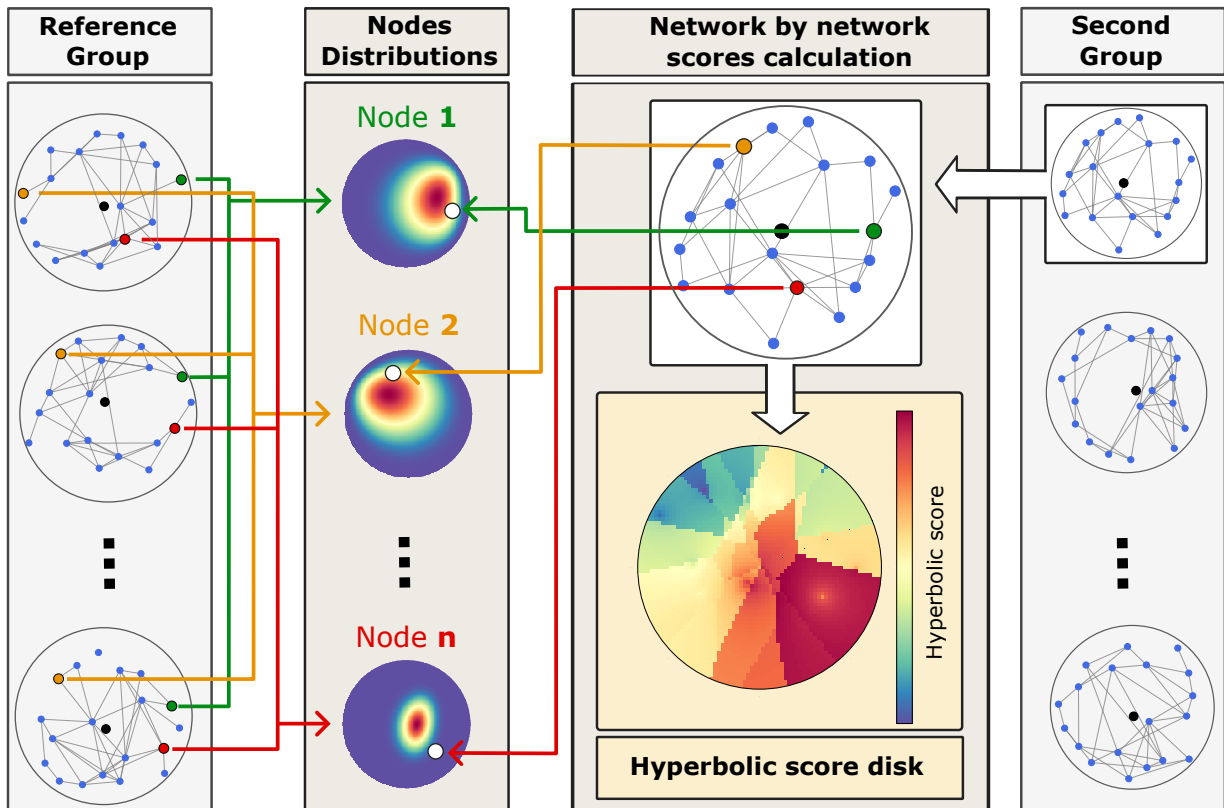


FIG. 1: Calculation of the Hyperbolic Score Disks. First, we computed the hyperbolic Gaussian distributions of the nodes from the reference group (interictal networks). The networks' nodes from the second group are then compared to these distributions, and a score is attributed to each node. Finally, the scores of the nodes are interpolated across the entire hyperbolic disk.

D. Discrimination in the Hyperbolic Score Disk

To ascertain whether there were any significant differences between the hyperbolic score disks of the preictal and interictal groups, a Student's t-test was employed. Firstly, all HSDs from the two groups were obtained. For a statistical cross-validation of the preictal-interictal networks separation, the two groups can be a subsample of the total number of disks. With the two groups defined, all pixels in the HSD are vectorized, and compared with a t-test to obtain a vector of t-values (one for each pixel of the disk), which can then be back-projected onto the original hyperbolic disk. Permutation tests were employed to provide an accurate approximation of the p_{value} for each pixel. These tests entailed randomly permuting individuals between the two groups and subsequently performing t-tests on the resulting groups to compare them with the original value. The region of interest (referred here to as the ROI) is the region of the disk where the p_{values} are the smallest, indicating the region of the disk where the two groups exhibit the greatest statistical divergence. An example of ROI is illustrated in Fig. 2.

E. Prospective forecasting

The model was trained using data from all previous days to predict the probability of a given network being in the preictal group (with a seizure within the next 24 hours). The training set was required to include at least one day from each group (preictal and interictal). Gaussian models were constructed from the embedded interictal networks, and the hyperbolic score disk was calculated for all networks in the training set. The two groups of HSD (interictal and preictal networks) are then compared, and a region of interest (ROI) is identified within the hyperbolic disk, as previously described. For each embedded network from the learning set, the median value of the pixels within the ROI is calculated and used as an independent variable for the prediction. As the connectivity matrices were available in multiple frequency bands, these steps were repeated for each frequency band. Each disk (30 per day) was assigned to the class of the day (with or without seizures) and was associated with a vector containing the median values of the ROIs for each frequency band. The aforementioned data were subsequently utilized to fit a logistic regression, thereby enabling a new network to be assigned a probability, p , of belonging to a preictal day. For each new day, the probability of belonging to the preictal class

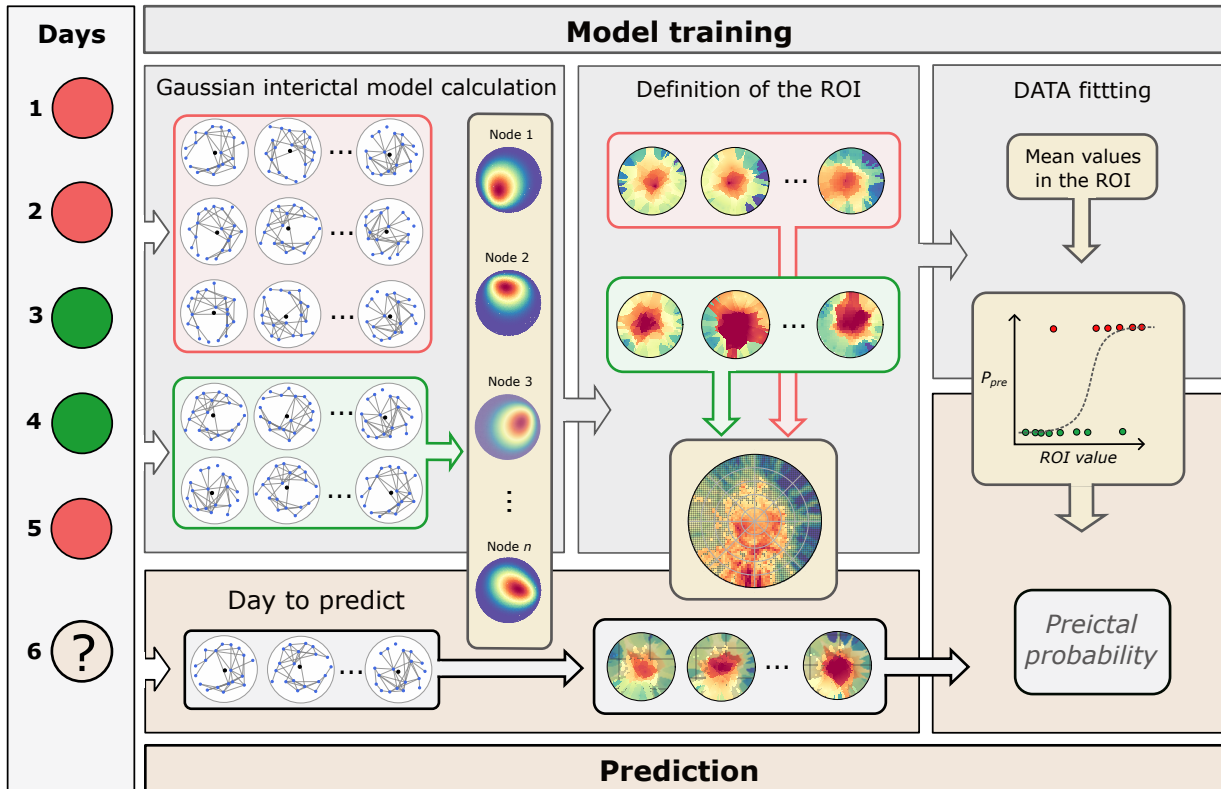


FIG. 2: Forecasting method for one patient and one frequency band. In this example, the aim is to forecast the seizure likelihood of networks from day 6 using data from days 1 to 5. To achieve this, Gaussian models are associated to all nodes using interictal networks from days 1 to 5. The region of the HSD where the two groups exhibit the largest statistical difference (ROI) is then defined. The values within this ROI are utilized to train a logistic regression model, which predicts the category of each network of the following day(s).

was calculated by averaging the probabilities associated with the 30 disks of the day. The combinations of bands with the highest prediction score, calculated using the training set of each patient, were then utilized in a logistic regression for the prediction of successive days. It is important to note that the selected combination of bands may differ between patients. The methodology for a single frequency band is illustrated in Fig. 2.

F. Evaluation of classification and forecasting performances

As connectivity patterns may be highly correlated between short epochs from the same daily recording, which could result in overestimated discrimination performances, we considered a leave-one-day-out cross-validation: for each patient, all 30 networks from a single day were assigned to the testing dataset, whereas the remaining data was used to train the algorithm. Once the model had been trained, it was tested on the data from the removed day, and its preictal probability were calculated. This process was repeated for all the days.

The discriminatory potential and forecasting performance of the model were evaluated based on several met-

TABLE I: Discrimination performances. Results indicate the mean values \pm the standard deviation over the patients. They are presented for each frequency band considered independently, and the final row displays those obtained from the best combination of bands in each patient.

Band	AUC Value	F1 score	Accuracy
δ	0.387 ± 0.35	0.33 ± 0.34	0.56 ± 0.28
θ	0.32 ± 0.29	0.29 ± 0.32	0.50 ± 0.22
α	0.623 ± 0.26	0.38 ± 0.27	0.62 ± 0.09
β	0.46 ± 0.40	0.39 ± 0.42	0.53 ± 0.33
Low γ	0.6675 ± 0.31	0.64 ± 0.16	0.75 ± 0.16
High γ	0.277 ± 0.35	0.28 ± 0.35	0.55 ± 0.21
Combined	0.932 ± 0.07	0.79 ± 0.18	0.85 ± 0.13

rics, including accuracy, recall, precision, F1-score, and the area under the receiver operating characteristic curve (AUC). Accuracy measures the proportion of correct predictions made by the learning model. Recall or sensitivity quantifies the model's ability to identify all relevant positives. Precision, also known as positive predictive value, assesses the model's ability to distinguish true positives

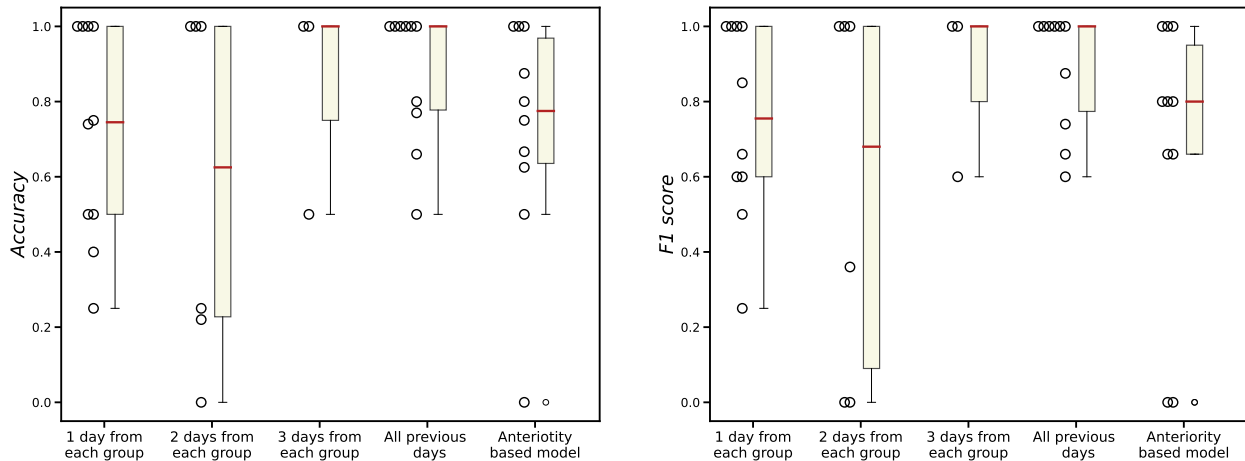


FIG. 3: Accuracy and F1 score results based on the minimum number of days from each class in the training set. Data are presented in scatter plots where each small circle represents a patient, and the red line indicates the median. The term “Anteriority-based model” refers to the method that bases its predictions on the immediate previous day’s state.

from false positives. To take into account the class imbalance of the dataset (i.e., the number of preictal days is lower compared to interictal epochs) we used here the F1-score, which is a weighted average of recall and precision. F1-score strikes a balance between minimizing false negatives and false positives, thereby ensuring a reliable assessment of the model’s effectiveness. Finally, the AUC, which ranges from 0.5 for a random classification to 1 for a perfect classification, provides a comprehensive assessment of the model’s performance.

To provide a comprehensive evaluation of our forecasting model we computed the Brier score (i.e., the mean squared error over every forecast; from 0 [perfect prediction] to 1 [worst prediction]) and the Brier skill score (BSS), which measures the improvement over a default prediction (given the limited number of recording sessions, the default probability of seizures was estimated as the proportion of the total preictal/interictal epochs for each patient), and take values from 0 (no improvement) to 1 (perfect forecasting), with negative values indicating worse performances than default predictions.

III. RESULTS

A. Discrimination of preictal networks

We first evaluated the ability of the proposed method to discriminate between interictal and preictal networks. Classification performances were assessed by AUC, the accuracy, and the F1-score and are presented in Tab. I. In general, the connectivity patterns associated with activities of separated frequency bands cannot distinguish between preictal and interictal days. Only networks estimated from low γ oscillations (30-49 Hz) performed bet-

ter than a random classifier. Nevertheless, classification performances considerably increased when the information from different frequency bands was combined for each patient: All patients reached AUCs of ≥ 0.78 (mean AUC = 0.93, mean F1 score = 0.79, and mean accuracy = 0.85). These findings suggest that the combination of the connectivity in different frequency bands conveys information that can distinguish preictal from interictal epochs.

B. Forecasting of upcoming seizure(s)

The forecasting method was first assessed by examining the number of days from each class in the training set. The results are presented in Fig. 3, which plots the accuracy and F1 score against the minimum number of days from each class in the training set. When only one day ($n = 1$) from each class was included in the training set, the average accuracy of prediction was 0.71 [min. 0.25, max. 1] and the mean F1-score was 0.75 [min. 0.25, max. 1]. However, these values increased considerably to 0.83 [min. 0.5, max. 1] for the accuracy and 0.87 [min. 0.61, max. 1] for the F1-score when the model was trained with three days from each class. When every day was predicted with a model trained with data from all previous days, performances reached the highest values of accuracy 0.87 and F1-score 0.89 (See Fig. 3). The use of different reference networks (from previous days) in the alignment of the embedded data yielded similar performances.

Fig. 4 presents the forecasting results for all patients when data from all the previous days were used for training the model. Patient-specific predictions were performed with the most discriminant combination of net-

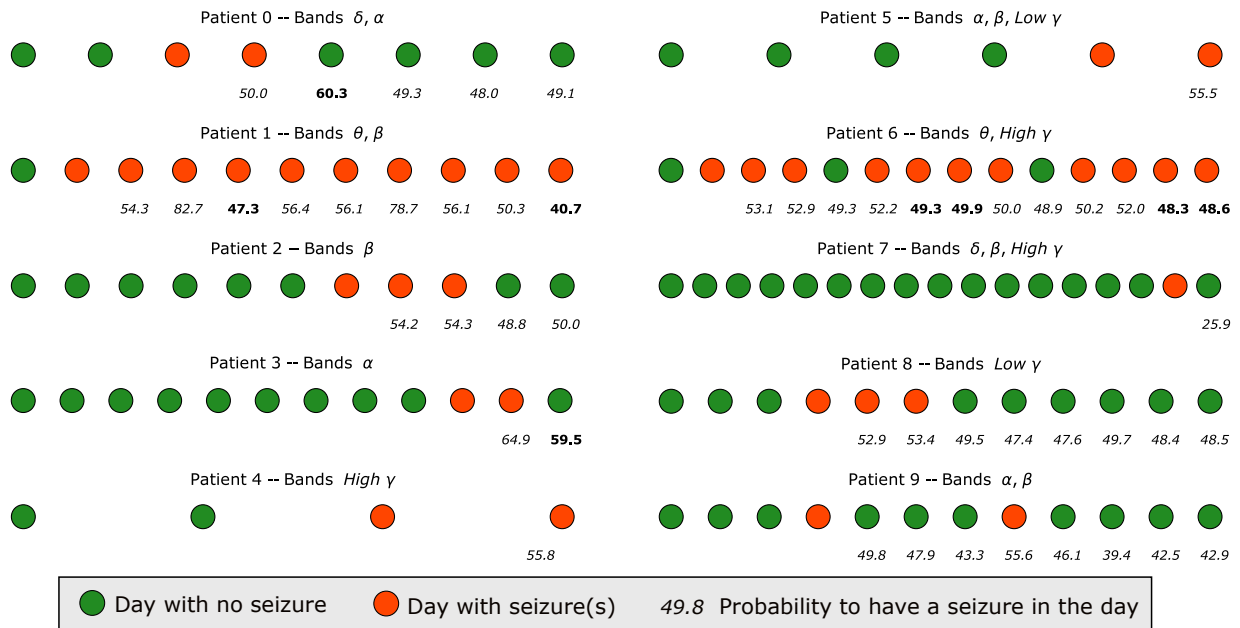


FIG. 4: Forecasting results for all patients using data from all previous days in the training model. Probabilities that give the wrong class to the day are highlighted in bold.

works in different frequency bands. Of the 28 preictal days (days with seizures), 22 (78.5%) were correctly predicted with a probability of $> 50\%$. False positive predictions were observed in only two of 23 (8.6%) interictal periods (in two patients), and they exclusively occurred after two consecutive days with seizures.

The efficacy of our method was evaluated in comparison to a basic anteriority-based model, which is a classifier that bases its predictions on the previous day's state. This simple model yielded an average accuracy value of 0.72, but this value could be overestimated as accuracy does not take into account the class imbalance (i.e., the relatively reduced number of preictal days). In this case, the F1-score, which combines precision and recall, provides a better assessment of model performance. Here, the anteriority-based model yielded a moderate F1-score of 0.67. Further, we noticed that this value was very close to that obtained with a non-informative (random), which yielded an averaged F1-score of 0.68 (for each patient, this non-informative model's F1-score can be estimated by $2p/(p+1)$, where p is the rate of preictal epochs).

Forecasting results were consistent with those of our previous study, in which we demonstrated that brain connectivity obtained from vigilance-controlled resting-state recordings could accurately predict the risk of upcoming seizures. [14]. The results, presented in Table. II, demonstrate the forecasting performance obtained for the distinct frequency bands when the prediction models for each day were trained with data from all preceding days. Combining information from different frequency bands yielded a good predictor with an average Brier score and BSS of 0.12 [min. = 0.003, max. = 0.48] and 0.36 [min. = -0.43, max. = 0.70], respectively. These values con-

firm that this prediction model performed better than a non-informative model to forecast the risk of upcoming seizure(s). We notice, however, that connectivity networks from the β and low γ band, also provided good predictors, in agreement with previous findings [14].

IV. DISCUSSION

This study provided empirical evidence supporting the hypothesis that hyperbolic spaces are suitable for representing complex brain connectivity patterns. This makes it a promising framework for accurately distinguishing between interictal and preictal states. In contrast to standard seizure prediction methods that track changes in EEG dynamics by analyzing long-term recordings [7, 33], our study confirmed that short and daily single resting-state recordings can reflect a pro-ictal state, at least at the daily level.

The classification performances demonstrated a high degree of discriminating power when the information from brain connectivity in different frequency bands was combined for each patient. The combination of networks from different frequency bands yielded the most accurate predictions (an accuracy of 85% and F1-score of 79%), but it is notable that connectivity networks from the beta and low gamma bands also demonstrated excellent forecasting results. For all patients, the predictive performance was enhanced by increasing the quantity of learning data. For each day, the optimal prediction was achieved when the models were recursively trained with networks from all preceding days. For these models, false positives were only detected in two patients, and

TABLE II: Forecasting performances. The given results are the averaged values over the patients \pm the standard deviation. The results are presented for each band considered independently and the final row displays the result for the best combination of bands for each patient. BS : Brier Score, BSS : Brier Skill Score.

Band	BS	BSS	F1 Score	Accuracy
δ	0.10 ± 0.12	0.40 ± 0.44	0.36 ± 0.38	0.49 ± 0.31
θ	0.08 ± 0.05	0.52 ± 0.41	0.53 ± 0.35	0.55 ± 0.27
α	0.08 ± 0.04	0.48 ± 0.41	0.44 ± 0.35	0.52 ± 0.20
β	0.08 ± 0.05	0.44 ± 0.41	0.67 ± 0.34	0.65 ± 0.33
Low γ	0.08 ± 0.06	0.46 ± 0.45	0.70 ± 0.31	0.74 ± 0.22
High γ	0.08 ± 0.06	0.50 ± 0.40	0.46 ± 0.35	0.55 ± 0.35
Combined	0.12 ± 0.12	0.36 ± 0.35	0.89 ± 0.14	0.87 ± 0.17

only occurred immediately after consecutive preictal periods. This may indicate a pro-ictal condition, in which seizures are more likely to occur after a day of seizures. However, homeostatic control mechanisms could prevent their emergence.

It should be noted that other non-Euclidean embeddings (e.g. spherical or elliptic), and that alternative dimensional reduction methods (e.g., Isomaps, Locally Linear embeddings [28]) can also be used. Similarly, representations in different hyperbolic spaces, such as Lorentz-Klein, d -dimensional Poincaré’s ball, or the half-space model, can be used as alternatives to Poincaré’s disk. Although other hyperbolic mappings (e.g., Mercator [25] HyperMap [34] or Hydra [35] among others) are alternatives to projecting brain networks into the 2D Poincaré disk, the coalescent embedding method used here encompasses various benefits. These include a short computational time and the absence of stochastic minimization procedures, thus preventing errors introduced by local minima.

Despite the good classification and prediction results, our study has some limitations. First, the vigilance-controlled resting-state iEEG recordings were obtained from hospitalized patients who were candidates for presurgical evaluation. Although no trivial correlations were found between the occurrence of seizures and the controlled medication tapering [14], the results cannot be directly generalized to out-of-hospital real-life conditions. Similarly, given the heterogeneity of electrode location among the patients, we cannot generalize a single unique prediction model. While a larger cohort of patients is necessary to map out the limits of the proposed approach, the results do suggest that the method has the potential to be a promising tool for the analysis of brain networks.

To summarize, our findings indicate that non-Euclidean embeddings of brain networks may offer more discriminative information for distinguishing between interictal and preictal states, thereby providing a promising tool for accurately forecasting the daily risk of upcoming seizure(s).

ACKNOWLEDGMENTS

M.G. acknowledges doctoral support from the Ecole Normale Supérieure de Lyon, France.

Appendix A: Hyperbolic Gaussian distribution

Let us consider an ensemble of points in the Poincaré’s disk. As in the case of the Euclidean space, the distribution of the points can be characterized by a barycenter and a covariance matrix. This information is sufficient to approximate the distribution by a two-dimensional Gaussian distribution.

1. Hyperbolic logarithmic and exponential maps

The logarithmic map $\text{Log}_u(v)$ provides a way to project a point $v \in \mathbb{D}$ (in complex coordinates) into the tangent space $T_u\mathbb{D}$ at the point u , as follows :

$$\text{Log}_u(v) = (1 - |u|^2) \text{atanh} \left(\left| \frac{v - u}{1 - \bar{u}v} \right| \right) e^{j\theta} \quad (\text{A1})$$

where $\theta = \arg \left(\frac{v - u}{1 - \bar{u}v} \right)$, and $\text{atanh}(\cdot)$ denotes to the inverse of the hyperbolic tangent function.

The exponential map $\text{Exp}_u(v)$ allows to do the inverse transformation, i.e. projecting a point $v \in T_u\mathbb{D}$ from the tangent space at u into the disk \mathbb{D} in the following way:

$$\text{Exp}_u(v) = \frac{(u + e^{j\theta}) e^{2\|v\|} + (u - e^{j\theta})}{(1 + \bar{u}e^{j\theta}) e^{2\|v\|} + (1 - \bar{u}e^{j\theta})} \quad (\text{A2})$$

where $\theta = \arg(v)$ and $\|v\| = \frac{|v|}{1 - |u|^2}$.

2. Hyperbolic barycenter computation

To estimate the barycenter of a set of points in the Poincaré disk, we used the algorithm presented in Ref. [32]. The algorithm converges to the barycenter of

the points by means of recursive projections in the tangent space. It iterates between the Poincaré disk and the tangent space until convergence is achieved. The algorithm is presented in Algorithm. 1.

3. Estimation of covariance matrix in the hyperbolic disk

To estimate the covariance matrix of a set of points z_i in the hyperbolic disk, we first calculated their barycenter u with the algorithm described above. The points distribution is then projected into the tangent space centered on the estimated barycenter \hat{z} of the points on $T_u\mathbb{D}$, using the logarithmic map $\text{Log}_{\hat{z}}(\cdot)$. In this Euclidean subspace, the barycenter is the point with coordinates $(0, 0)$ and the covariance matrix can finally be calculated as follows: $V_{\hat{z}} = \text{Covariance}([\text{Log}_{\hat{z}}(z_i)]^T)$

Algorithm 1: Barycentre computation

Data:

$Z = \{z_i, 1 \leq i \leq n\}$: complex coordinates of the points in the Poincaré's disk,

z_{init} : Barycentre initialisation (complex coordinates),

τ_b : step size (strictly positive),

d_{thres} : threshold of convergence for d .

Result:

\hat{z} : numerical approximation of the barycenter (in complex coordinates)

$\hat{z} \leftarrow z_{init}$;

$d \leftarrow 1e6$;

$N \leftarrow n$;

while $d \geq d_{thres}$ **do**

$\mu \leftarrow \frac{2}{n} \sum_{i=1}^n \text{Log}_{\hat{z}}(z_i)$;

$\hat{z} \leftarrow \text{Exp}_{\hat{z}}(\tau_b \mu)$;

$d \leftarrow \sqrt{\frac{|\mu|^2}{(1-|z|^2)^2}}$;

end

- [1] S. Boccaletti, V. Latora, Y. Moreno, M. Chavez, and D.-U. Hwang, Complex networks: Structure and dynamics, *Physics Reports* **424**, 175 (2006).
- [2] J. C. Reijneveld, S. C. Ponten, H. W. Berendse, and C. J. Stam, The application of graph theoretical analysis to complex networks in the brain, *Clinical Neurophysiology* **118**, 2317 (2007).
- [3] E. Bullmore and O. Sporns, Complex brain networks: graph theoretical analysis of structural and functional systems, *Nature Reviews Neuroscience* **10**, 186 (2009).
- [4] F. De Vico Fallani, J. Richiardi, M. Chavez, and S. Achard, Graph analysis of functional brain networks: practical issues in translational neuroscience, *Philosophical Transactions of the Royal Society B: Biological Sciences* **369**, 20130521 (2014).
- [5] M. A. Kramer and S. S. Cash, Epilepsy as a disorder of cortical network organization, *The Neuroscientist* **18**, 360 (2012), pMID: 22235060.
- [6] E. van Diessen, S. J. H. Diederer, K. P. J. Braun, F. E. Jansen, and C. J. Stam, Functional and structural brain networks in epilepsy: What have we learned?, *Epilepsia* **54**, 1855 (2013).
- [7] L. Kuhlmann, K. Lehnertz, M. P. Richardson, B. Schelter, and H. P. Zaveri, Seizure prediction — ready for a new era, *Nature Reviews Neurology* **14**, 618 (2018).
- [8] M. Boguñá, I. Bonamassa, M. De Domenico, S. Havlin, D. Krioukov, and M. Á. Serrano, Network geometry, *Nature Reviews Physics* **3**, 114 (2021).
- [9] A. Allard and M. Á. Serrano, Navigable maps of structural brain networks across species, *PLoS Computational Biology* **16**, 1 (2020).
- [10] M. Zheng, A. Allard, P. Hagmann, Y. Alemán-Gómez, and M. Á. Serrano, Geometric renormalization unravels self-similarity of the multiscale human connectome, *Proceedings of the National Academy of Sciences* **117**, 20244 (2020).
- [11] T. Hofmann, B. Schölkopf, and A. J. Smola, Kernel methods in machine learning, *The Annals of Statistics* **36**, 1171 (2008).
- [12] M. Le Van Quyen, J. Soss, V. Navarro, R. Robertson, M. Chavez, M. Baulac, and J. Martinerie, Preictal state identification by synchronization changes in long-term intracranial eeg recordings, *Clinical Neurophysiology* **116**, 559 (2005).
- [13] P. Van Mierlo, M. Papadopoulou, E. Carrette, P. Boon, S. Vandenberghe, K. Vonck, and D. Marinazzo, Functional brain connectivity from eeg in epilepsy: Seizure prediction and epileptogenic focus localization, *Progress in Neurobiology* **121**, 19 (2014).
- [14] L. Cousyn, R. B. Messaoud, K. Lehongre, V. Frazzini, V. Lambrecq, C. Adam, B. Mathon, V. Navarro, and M. Chavez, Daily resting-state intracranial eeg connectivity for seizure risk forecasts, *Epilepsia* **64**, e23 (2023).
- [15] M. Nickel and D. Kiela, Learning continuous hierarchies in the Lorentz model of hyperbolic geometry, in *Proceedings of the 35th International Conference on Machine Learning*, Proceedings of Machine Learning Research, Vol. 80, edited by J. Dy and A. Krause (PMLR, 2018) pp. 3779–3788.
- [16] C. Saxena, T. Liu, and I. King, A survey of graph curvature and embedding in non-euclidean spaces, in *Neural Information Processing*, edited by H. Yang, K. Pasupa, A. C.-S. Leung, J. T. Kwok, J. H. Chan, and I. King (Springer International Publishing, 2020) pp. 127–139.
- [17] T. O. Sharpee, An argument for hyperbolic geometry in neural circuits, *Current Opinion in Neurobiology* **58**, 101 (2019), computational Neuroscience.
- [18] F. De Vico Fallani, V. Latora, and M. Chavez, A topological criterion for filtering information in complex brain networks, *PLoS Computational Biology* **13**, 1 (2017).
- [19] C. Stam, P. Tewarie, E. Van Dellen, E. Van Straaten, A. Hillebrand, and P. Van Mieghem, The trees and the forest: characterization of complex brain networks with

- minimum spanning trees, *International Journal of Psychophysiology* **92**, 129 (2014).
- [20] A. Cacciola, A. Muscoloni, V. Narula, A. Calamuneri, S. Nigro, E. A. Mayer, J. S. Labus, G. Anastasi, A. Quattrone, A. Quartarone, D. Milardi, and C. V. Cannistraci, Coalescent embedding in the hyperbolic space unsupervisedly discloses the hidden geometry of the brain (2017), arXiv:1705.04192 [q-bio.NC].
- [21] S. Gao, G. Mishne, and D. Scheinost, Poincaré embedding reveals edge-based functional networks of the brain, in *Medical Image Computing and Computer Assisted Intervention – MICCAI 2020*, edited by A. L. Martel, P. Abolmaesumi, D. Stoyanov, D. Mateus, M. A. Zuluaga, S. K. Zhou, D. Racocanu, and L. Joskowicz (Springer International Publishing, 2020) pp. 448–457.
- [22] W. Whi, S. Ha, H. Kang, and D. S. Lee, Hyperbolic disc embedding of functional human brain connectomes using resting-state fMRI, *Network Neuroscience* **6**, 745 (2022).
- [23] C. Saxena, T. Liu, and I. King, A survey of graph curvature and embedding in non-euclidean spaces (Springer Science and Business Media Deutschland GmbH, 2020) pp. 127–139.
- [24] M. Nickel and D. Kiela, Poincaré embeddings for learning hierarchical representations, in *Advances in Neural Information Processing Systems (NIPS 2017)*, Vol. 30, edited by I. Guyon, U. V. Luxburg, S. Bengio, H. Wallach, R. Fergus, S. Vishwanathan, and R. Garnett (Curran Associates, Inc., Long Beach, CA, USA, 2017) pp. 6341–6350.
- [25] G. García-Pérez, A. Allard, M. Á. Serrano, and M. Boguná, Mercator: uncovering faithful hyperbolic embeddings of complex networks, *New Journal of Physics* **21**, 123033 (2019), 118.
- [26] A. Muscoloni, J. M. Thomas, S. Ciucci, G. Bianconi, and C. V. Cannistraci, Machine learning meets complex networks via coalescent embedding in the hyperbolic space, *Nature Communications* **8**, 1615 (2017).
- [27] A. Longhena, M. Guillemaud, and M. Chavez, Detecting local perturbations of networks in a latent hyperbolic embedding space, *Chaos: An Interdisciplinary Journal of Nonlinear Science* **34**, 063117 (2024), https://pubs.aip.org/aip/cha/article-pdf/doi/10.1063/5.0199546/19978086/063117_1_5.0199546.pdf.
- [28] U. von Luxburg, A tutorial on spectral clustering, *Statistics and Computing* **17**, 395 (2007).
- [29] M. Belkin and P. Niyogi, Laplacian eigenmaps for dimensionality reduction and data representation, *Neural computation* **15**, 1373 (2003).
- [30] M. Kitsak, I. Voitalov, and D. Krioukov, Link prediction with hyperbolic geometry, *Physical Review Research* **2**, 43113 (2020).
- [31] F. Gürsoy, M. Haddad, and C. Bothorel, Alignment and stability of embeddings: measurement and inference improvement, *Neurocomputing* **553**, 126517 (2023).
- [32] T. Gerald, H. Zaatiti, H. Hajri, N. Baskiotis, and O. Schwander, From node embedding to community embedding: A hyperbolic approach (2020), arXiv:1907.01662 [cs.LG].
- [33] S. Beniczky, P. Karoly, E. Nurse, P. Ryvlin, and M. Cook, Machine learning and wearable devices of the future, *Epilepsia* **62**, S116 (2021).
- [34] F. Papadopoulos, C. Psomas, and D. Krioukov, Network mapping by replaying hyperbolic growth, *IEEE/ACM Transactions on Networking* **23**, 198 (2014).
- [35] M. Keller-Ressel and S. Nargang, Hydra: a method for strain-minimizing hyperbolic embedding of network-and distance-based data, *Journal of Complex Networks* **8**, cnaa002 (2020).